Effects of MnO$_2$ of different structures on activation of peroxymonosulfate for bisphenol A degradation under acidic conditions

Jianzhi Huang[a], Yifan Dai[b], Kevin Singewald[c], Chung-Chiun Liu[b], Sunil Saxena[c], Huichun Zhang[a],*

[a] *Department of Civil Engineering, Case Western Reserve University, United States*
[b] *Department of Chemical & Biomolecular Engineering, Case Western Reserve University, United States*
[c] *Department of Chemistry, University of Pittsburgh, United States*

HIGHLIGHTS

- MnO$_2$ structures affected activation of peroxymonosulfate for BPA degradation.
- Three crystalline MnO$_2$ were more reactive than less crystalline δ-MnO$_2$.
- Reactivity of crystalline MnO$_2$ correlated with Mn AOS, Mn(III)%, and conductivity.
- Direct oxidation by MnO$_2$ was important in BPA degradation in acidic conditions.
- Both radical and non-radical mechanisms were involved in the catalytic oxidation.

GRAPHICAL ABSTRACT
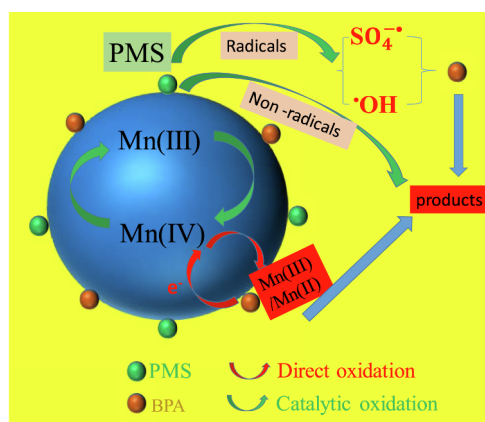
ARTICLE INFO

ABSTRACT

MnO$_2$ with various structures, including three tunnel structures (α-, β-, γ-MnO$_2$) and a layered structure (δ-MnO$_2$), were synthesized and investigated for peroxymonosulfate (PMS) activation. The effects of different structured MnO$_2$ on PMS activation in contaminant degradation, as quantified by the pseudo-first order rate constants of bisphenol A (BPA) oxidation, followed the order: α-MnO$_2$ > γ-MnO$_2$ > β-MnO$_2$ > δ-MnO$_2$. Results showed that under acidic conditions, BPA was degraded by both catalytic oxidation by PMS-MnO$_2$ and direct oxidation by MnO$_2$, and the relative importance of the two mechanisms differed for different MnO$_2$. The direct oxidation accounted for 25.2, 7.4, 34.1, and 94.5% of the total reactivity of α-, β-, γ-, and δ-MnO$_2$, respectively. Physicochemical properties of MnO$_2$ including crystal structure, morphology, surface Mn oxidation states, surface area, oxygen species and conductivity were characterized and correlated with the catalytic reactivity. The results demonstrated that the crystallinity of MnO$_2$ was the dominant factor in the catalytic reactivity, resulting in the lowest reactivity for the least crystalline δ-MnO$_2$. For the crystalline MnO$_2$, the catalytic reactivity linearly correlated with Mn average oxidation state, Mn(III) content, and conductivity. Electron spin resonance (ESR) and quenching experiments with ethanol and *tert*-butanol suggested that sulfate radicals (SO$_4$$^{\cdot-}$) were the dominant radicals in the systems, while hydroxyl radicals ($\cdot$OH) played a minor role. In addition, nonradical mechanisms such as singlet oxygen (^{1}O$_2$) also contributed to the BPA degradation,

---

* Corresponding author.
  E-mail address: hjz13@case.edu (H. Zhang).

especially when δ-MnO$_2$ was the catalyst. These findings offered new insights into the contaminant degradation mechanisms in PMS-MnO$_2$ and provided guidance to develop cost-effective catalysts for water/wastewater treatment.
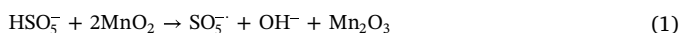
1. Introduction

Sulfate radical-based advanced oxidation processes (AOPs) have been an important technology in the treatment of a wide range of environmental pollutants [1,2]. Sulfate radicals produced from species such as peroxymonosulfate (PMS) have received increasing attention because they have a high redox potential (2.5–3.1 V), exist under a wide range of solution pH [3], and have a longer life time than hydroxyl radical (30–40 μs vs 20 ns) [1]. Sulfate radicals can be generated by activation of PMS by heat, metal ions, UV, activated carbon, and metal oxides [4].

Many heterogeneous transition metal catalysts have been reported to activate PMS, including Co-, Cu-, Ag-, and Ru-based catalysts [4]. Compared to transition metal catalysts, Mn-based catalysts have their own advantages including high natural abundance, low toxicity, and environmental friendliness [5,6]. Manganese oxides have attracted a great deal of attention due to their promising applications in oxidation reactions in environmental and energy fields, e.g., ozone decomposition [7], photocatalytic oxidation of organic pollutants [8], and decomposition of hydrogen peroxide [9]. Researchers have synthesized several new effective manganese oxides, like octahedral molecular sieve [10] and α-Mn$_2$O$_3$@α-MnO$_2$-500 [11], as the catalysts for the activation of PMS. In addition, the effects of a number of factors of manganese oxides have been investigated, including phase structure [12], oxidation state [13], and different shapes [14]. For example, Saputra et al. reported that Mn$_2$O$_3$ was the best catalyst in activating PMS to produce sulfate radicals for phenol degradation, with the sequence of the catalytic activity as Mn$_2$O$_3$ > MnO > Mn$_3$O$_4$ > MnO$_2$, which correlated with Mn oxidation state and oxygen mobility on the catalysts [13]. In addition, α-Mn$_2$O$_3$ with cubic, octahedral and truncated-octahedral shapes have been synthesized and tested in degradation of phenol [14]. The authors found that cubic α-Mn$_2$O$_3$ exhibited the highest reactivity due to its high surface area and surface atoms arrangement.

The catalytic reactivity of MnO$_2$ in many applications is highly dependent on their morphology and phase structures. For instance, Zhang et al. found that δ-MnO$_2$ was more reactive than α-, β-, and γ-MnO$_2$ in the catalytic oxidation of formaldehyde, due to its layer structure and active lattice oxygen species [15]. It has also been shown that electrochemical water oxidation strongly depended on the crystallographic structure of the MnO$_2$ in the order of α- > β- > δ-MnO$_2$, which can be ascribed to factors including mixed Mn valence and lower charge transfer resistance [16].

Given that the phase structure of MnO$_2$ strongly affects its catalytic reactivity in many applications, as examples shown above, it is likely that MnO$_2$ with different structures would also have different catalytic reactivity in PMS activation. It is generally believed that sulfate radicals and hydroxyl radicals are generated when PMS is activated by MnO$_2$ [1]:

$$HSO_5^- + 2MnO_2 \rightarrow SO_5^{\cdot-} + OH^- + Mn_2O_3 \tag{1}$$

$$HSO_5^- + Mn_2O_3 \rightarrow SO_4^{\cdot-} + H^+ + 2MnO_2 \tag{2}$$

$$SO_4^{\cdot-} + H_2O \rightarrow HO^{\cdot} + H^+ + SO_4^{2-} \tag{3}$$

However, there has been little effort to comprehensively understand the structure effects of MnO$_2$ on PMS activation. To the best of the authors' knowledge, only one previous study demonstrated that α-MnO$_2$ exhibited better activity than β- and γ-MnO$_2$ in phenol oxidation [12]. However, the study only investigated tunnel structured MnO$_2$ (α-, β-, and γ-MnO$_2$) without considering layer structured δ-MnO$_2$. δ-MnO$_2$

resembles the most abundant manganese oxide structure in the natural environment. The authors suggested a few possible reasons for α-MnO$_2$ to have the highest catalytic reactivity (e.g., tunnel size, oxygen liability, MnO$_6$ edges); however, no experimental data were provided to prove the hypothesis. In addition, the oxidative reactivity of MnO$_2$ itself is significantly pH dependent [17]. The addition of 2 g/L Oxone into the solution decreased the pH to around 2.41, under which the direct oxidation of contaminants by MnO$_2$ was greatly enhanced [6,17]. It is likely that the observed phenol degradation by PMS-MnO$_2$ under such acidic conditions not only resulted from the catalytic oxidation by sulfate and hydroxyl radicals as reported, but also from strong direct oxidation by MnO$_2$, which was overlooked in that work [12].

Surprisingly, we found that many previous papers using manganese-based catalysts to activate PMS failed to consider the contribution of direct oxidation by manganese oxides at acidic pH, and simply attributed the total reactivity to catalytic reactivity [12,13,18–21]. As a result, the conclusions of these previous papers will need to be re-examined because we found that the direct oxidative reactivity of manganese oxides at acidic pH is very important for some structured MnO$_2$, as will be demonstrated later. Moreover, the activation mechanism of PMS by different structured manganese dioxide (MnO$_2$) has not been well studied. Therefore, it is necessary to comprehensively investigate the effects of structured MnO$_2$ on the activation of PMS and re-examine some of the conclusions previously reported on PMS-MnO$_2$.

Here, we synthesized four different structured MnO$_2$ (α, β, γ and δ) and systematically evaluated their performance in the activation of PMS for BPA degradation. The direct oxidation of BPA by different phase structures of MnO$_2$ has been reported in our recent paper [22]; therefore, the current work focused on their catalytic reactivity, although direct oxidation also occurred under the employed reaction conditions. To better compare the reactivity of different MnO$_2$ phase structures in direct oxidation versus in PMS activation, the same types of α, β, γ and δ-MnO$_2$ were employed. BPA is one of the ubiquitous endocrine disruptors in engineered and natural environments [23], and was employed as a chemical probe for the reactivity of PMS-MnO$_2$. Different techniques, such as Scanning Electron Microscopy (SEM), Transmission Electron Microscopy (TEM), X-ray Powder Diffraction (XRD), X-ray photoelectron spectroscopy (XPS) and Electrochemical Impedance Spectroscopy (EIS), were used to study the oxide structural and surface properties, which were then used to correlate with the observed catalytic reactivity. Electron spin resonance (ESR) and chemical quenching experiments with ethanol and *tert*-butyl alcohol (TBA) were also conducted to understand the possible oxidation mechanisms in the system, including both radical and nonradical mechanisms.

2. Material and methods

2.1. Chemicals

All chemicals were used as received. Chemicals, including potassium permanganate (KMnO$_4$), manganese acetate tetrahydrate (Mn(Ac)$_2$·4H$_2$O), ammonium persulfate ((NH$_4$)$_2$S$_2$O$_8$), manganese sulfate monohydrate (MnSO$_4$·H$_2$O), bisphenol A (BPA), potassium hydroxide (KOH), HCl (trace metal-grade concentrated), ethanol (CH$_3$CH$_2$OH), sodium hydroxide (NaOH), sodium acetate, *tert*-butyl alcohol (TBA), methanol of HPLC grade, furfuryl alcohol (FFA), 5,5-dimethylpyrroline-N-oxide (DMPO), 2,2,6,6-tetramethyl-4-piperidinol (TMP) and Oxone (2KHSO$_5$·KHSO$_4$·K$_2$SO$_4$) were obtained from Fisher or SigmaAldrich at the highest available purity.

2.2. MnO$_2$ synthesis

We have previously synthesized different phase structures of MnO$_2$ for their direct oxidation in our recent paper [22]. Here, we re-synthesized these MnO$_2$ for the activation of PMS. The details of the synthesis methods are shown in Text S1 in the Supplementary Material (SM).

2.3. Catalytic degradation experiments

All experiments were conducted in duplicates in amber bottles (50 mL) on a stir plate at room temperature. Typically, MnO$_2$ (0.05 g/L) from stock solution was first added into ultrapure water and sonicated for 10 min, followed by adding BPA (6 μM) and Oxone (1 mM) to initiate the reaction. The addition of Oxone yielded a solution pH of 3.07. To be comparable with the literature data, we did not adjust the solution pH either. For direct oxidation experiments (without adding Oxone), pH of the solution containing MnO$_2$ (0.05 g/L) was initially adjusted to 3.07 with HCl, and then BPA was added to initiate the reaction. 0.5 mL of samples were collected at predetermined time intervals and then mixed with 0.5 mL methanol to quench the reaction. After that, the mixed solution was filtered into HPLC vials for further analysis by an Agilent 1260 Infinity II reversed phase high performance liquid chromatography (HPLC). Quenching experiments were conducted by adding a large amount of quenching agents namely ethanol and TBA (more details in Text S2). The HPLC mobile phase was methanol and 0.1% acetic acid (v/v 57:43) at the flow rate of 1 mL/min. Rate constants (k) of BPA degradation were calculated using the pseudo first-order kinetics. The dissolved Mn(II) in the solution was analyzed by a Varian SpectrAA 220FS atomic absorption spectrometer.

2.4. Characterization

We have characterized many properties of these MnO$_2$ in our previous paper [22]; however, since we re-synthesized these MnO$_2$, we characterized these new MnO$_2$ again and all the obtained physical-chemical properties are similar to the previous work. Specifically, X-ray diffraction (XRD) spectra were acquired from a Bruker D8 Advance Powder X-ray diffraction using Cu-Kα radiation at 40 kV and a 40 mA. The Brunauer-Emmett-Teller (BET) surface areas were measured on a Micromeritics TriStar II instrument. Surface elemental contents of different structured MnO$_2$ were analyzed by X-ray photoelectron spectroscopy (XPS, PHI VersaProbe 5000). Data analysis and curve fitting were conducted using MultiPak XPS software, following previous work [22,24]. Morphology and elemental analysis were obtained by Scanning electron microscopy (SEM) (FEI Quanta 400F) with an energy dispersive X-ray (EDX) detector and high-resolution transmission electron microscopy (HRTEM) (Tecnai TF30 ST). Fourier-transform infrared spectra (FTIR) of the samples were carried out on a Cary 630 spectrometer in the range of 600–4000 cm^{-1}. Electrochemical impedance spectroscopy (EIS) was examined using a CHI 660E Electrochemical Workstation operated in a standard three-electrode configuration using phosphate buffer (0.5 M) at room temperature. The bulk Mn average oxidation state (AOS) of different structured MnO$_2$ was determined by the chemical titration method following a previous study [25].

The continuous wave (CW) ESR experiments were performed at X-band (9.87 GHz) in a Bruker ElexSys E580 CW/FT spectrometer. Samples were drawn into Pyrex capillaries and placed into a Bruker ER4122 SHQE-W1 high-resolution resonator. These experiments were performed at room temperature (294 ± 1 K). The center field was set to 3512 G with a 150 G sweep width at a microwave power 15.00 mW. The modulation amplitude was set to 1 G, modulation frequency was 100 kHz, and conversion time was 20.48 ms. Each CW spectrum was collected for 1024 data points.

3. Results and discussion

3.1. Characterization of MnO$_2$

Powder X-ray diffraction (pXRD) patterns of the as-prepared manganese oxides are shown in Fig. S1. They agree with the pXRD patterns in the inorganic crystallographic database, with α-MnO$_2$ (JCPDS 29-1020), β-MnO$_2$ (JCPDS 24-0735), γ-MnO$_2$ (JCPDS 14-0644) and δ-MnO$_2$ (JCPDS 80-1098). δ-MnO$_2$ demonstrated broad diffraction feature, indicating that δ-MnO$_2$ is less crystalline, which is also confirmed in the HRTEM images with partially disordered lattice lines (Fig. 1).

SEM and TEM images have been obtained to observe the morphologies of different MnO$_2$ (Figs. 1 and S2). SEM images of α-MnO$_2$ demonstrated that it is nanofiber clusters, which is more obvious in the TEM image with the diameters 5–20 nm and the lengths around 60–120 nm. The HRTEM image shows that the interplanar distance of α-MnO$_2$ is 0.692 nm, corresponding to the (1 1 0) planar spacing, indicating the material is well ordered. β-MnO$_2$ in both SEM and TEM images were observed to be nanorods, with the diameters 0.2–0.4 μm and the lengths 1–2 μm. The interplanar distance of β-MnO$_2$ in HRTEM is 0.306 nm, corresponding to (1 1 0) planes of β-MnO$_2$, indicating β-MnO$_2$ is highly crystalline. γ-MnO$_2$ in TEM shows a nanofiber structure, with the diameters 10–30 nm and the lengths 1–2 μm. γ-MnO$_2$ in the SEM image shows that the nanofibers accumulate together to form a sphere with the diameter around 4 μm. The interplanar distance of γ-MnO$_2$ is 0.398 nm, corresponding to (1 2 0) facets, suggesting γ-MnO$_2$ is well crystalline. δ-MnO$_2$ did not display clear interparticle boundaries,
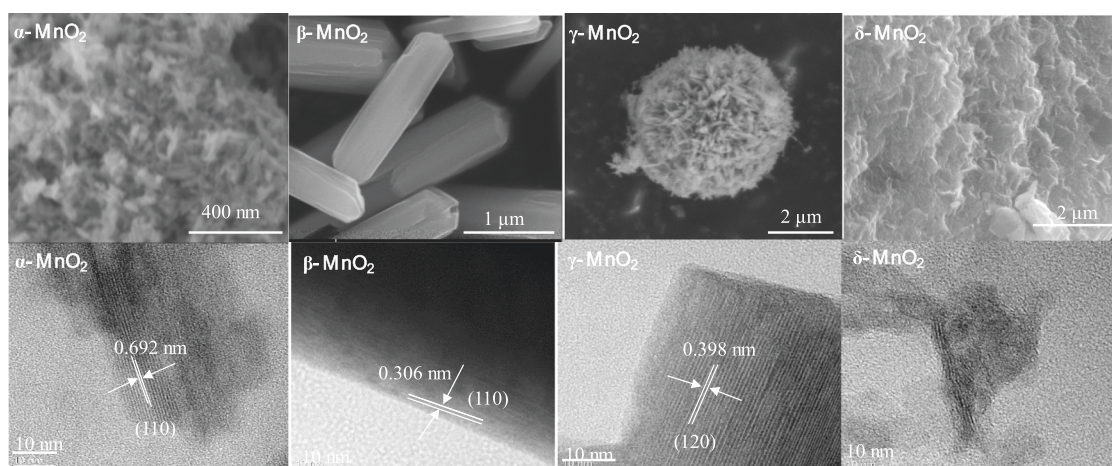
Fig. 1. SEM and HRTEM images of different structures of MnO$_2$.

just piles of layers. In addition, its interplanar distance is not clear compared to other structured MnO_2, indicating that δ-MnO_2 is less crystalline.

3.2. Catalytic activity of different MnO_2

The catalytic performance of different structured MnO_2 is shown in Fig. 2. The rate constants (k) of BPA degradation were calculated using the pseudo first-order kinetics (Eq. (4))

$$ln\left(\frac{C}{C_0}\right) = -kt \qquad (4)$$

where k is the rate constant, C_0 is the initial BPA concentration, and C is the BPA concentration at time (t).

Preliminary experiments showed that there was no BPA degradation without adding MnO_2, indicating there was no thermal activation of PMS, which is similar to previous research [12]. In addition, we found that there was negligible adsorption of BPA on MnO_2 within the experimental periods (10 min) (data not shown). BPA degradation by PMS in the presence of α-MnO_2 was almost completed (92%) in 10 min, followed by γ-MnO_2 (88%), β-MnO_2 (58%) and δ-MnO_2 (42%) (Fig. 2a). BPA degradation followed the pseudo first order kinetics. As shown in Fig. 2b, the total reaction rate constant (k_{tr}) decreased in the order: α-MnO_2 > γ-MnO_2 > β-MnO_2 > δ-MnO_2.

As mentioned in Introduction, the solution pH in the control experiments of many previous papers using manganese oxides to activate PMS was not the same as that in the reactors with PMS, as the addition of Oxone would significantly lower the solution pH but the control reactions with the Mn oxides were only maintained at near circumneutral pH [11–14,18,19]. Given the much lower reactivity of Mn oxides under neutral pH, it is not surprising that the Mn oxide controls were found non-reactive in those studies. In our experiments, 1 mM Oxone was added into the reactor, which resulted in a final pH 3.07. Unlike previous studies, we adjusted the pH to 3.07 for the control experiments. As shown in Fig. 2b, the ratio of k_{or}/k_{tr} is 25.2, 7.4, 34.1, and 94.5% for α-MnO_2, β-MnO_2, γ-MnO_2, and δ-MnO_2, respectively, indicating that direct oxidation played an important role in the total degradation, especially for δ-MnO_2.

The differences in k_{or} of different structured MnO_2 may result from different factors, such as Mn(III) content, surface area, surface adsorbed oxygen species, conductivity, and average Mn oxidation state, as already reported [22]. For δ-MnO_2 in our reaction system, the comparable k_{tr} vs. k_{or} suggests that the major role of Oxone was to lower the solution pH (just like a general acid), which led to enhanced direct oxidative reactivity of δ-MnO_2. While for α-, β- and γ-MnO_2, the

catalytic oxidation (k_{cr}) was more important (Fig. 2b), the reasons of which will be discussed in the following sections. Therefore, the proposed reaction mechanisms in the previous papers using manganese oxides to activate PMS without proper pH control [12–14,18,19] should be reinvestigated if they only considered the catalytic and adsorption role of the manganese oxides, but ignored their oxidant role at acidic conditions.

In addition, previous studies have shown that Mn(II) can activate PMS to degrade organic contaminants, although the reaction was very slow [2,26]. We also obtained similar results. In the PMS/MnO_2 systems, the maximum amount of Mn(II) leached into solution was small (< 0.37 ppm) during the reaction period of 10 min. Preliminary results showed that the degradation of BPA in the mixtures of Oxone and Mn (II) (0.37 ppm) was negligible under our experimental conditions (Fig. S3), indicating that we do not need to consider the contribution of PMS activation by the leached Mn(II) ions.

3.3. Effect of crystallinity of MnO_2

We originally thought δ-MnO_2 would be more reactive in PMS activation than tunnel structured MnO_2 because it has more accessible active sites [22]. However, the results suggest that δ-MnO_2 was less catalytically reactive than the tunnel structured MnO_2, even though its surface area is about 6 times larger than that of β-MnO_2. This is different from previous research showing that δ-MnO_2 had higher catalytic reactivity (should be *total reactivity instead*) than that of α-MnO_2 [18]. However, this paper failed to consider the contribution of direct oxidation, which made it difficult to compare the catalytic reactivity. δ-MnO_2 demonstrating less catalytic reactivity than the tunnel structured MnO_2 has been reported in other applications in previous studies [27,28]. For instance, Kim et al. found that compared with α-, β-, and γ-MnO_2, δ-MnO_2 was the least catalytically reactive in the decomposition of H_2O_2, which was ascribed to its low crystallinity and the exposed low-index planes that have lower surface energies [27].

Saputra et al. believed that the crystalline structure of MnO_2 (based on XRD) was more important than surface area and pore structure in activating PMS for phenol degradation [29]. Here, we synthesized another δ-MnO_2-1 and an amorphous MnO_2 (AMO) (Text S1) to test their activation of PMS to indirectly investigate the importance of crystallinity of MnO_2. XRD showed that both of them have poor crystallinity (Fig. S4). As shown in Fig. 3, the two δ-MnO_2 and the AMO all demonstrated total k_{tr} being comparable to the oxidative k_{or}, indicating that these two manganese oxides and the δ-MnO_2 had low catalytic reactivity. There might be several reasons for this phenomenon. First, δ-MnO_2 mainly exposes low-index planes that have lower surface
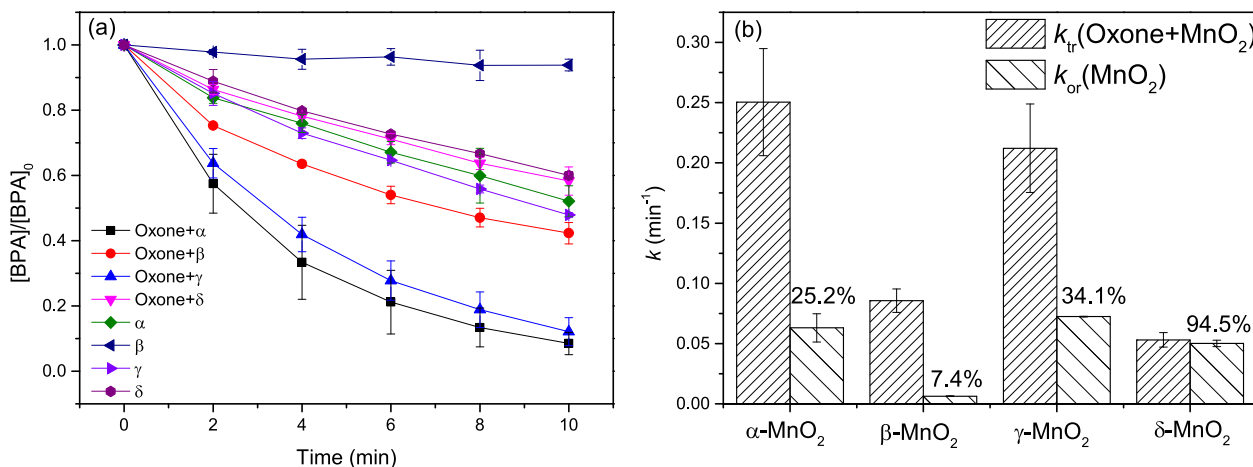

Fig. 2. (a) BPA degradation by different structures of MnO_2; (b) pseudo-first-order reaction rate constants of BPA degradation by Oxone-MnO_2 (k_{tr}) and by MnO_2 (k_{or}) at acidic pH. Reaction conditions: [BPA] = 6 μM, MnO_2 = 0.05 g/L, Oxone = 1 mM, and pH = 3.07 ± 0.04.
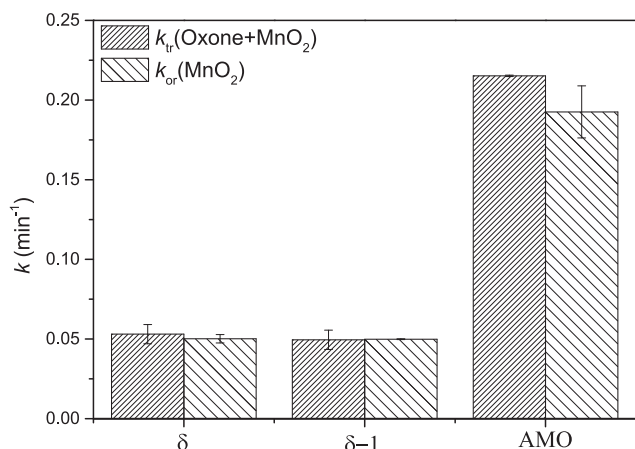
Fig. 3. BPA degradation by PMS in the presence of MnO_2. Reaction conditions: [BPA] = 6 μM, MnO_2 = 0.05 g/L, Oxone = 1 mM, and pH = 3.07 ± 0.04.

energies [27,30], thus less surface reactive compared with tunnel structured MnO_2. Second, previous studies have shown that Mn has six coordination sites, and coordinately unsaturated metal centers usually have superior catalytic reactivity [31,32]. However, the Mn in the dominantly exposed (0 0 1) facet of δ-MnO_2 are 6-fold coordinated to oxygen in a coordinately saturated environment [30], likely resulting in the lower catalytic reactivity. Therefore, δ-MnO_2 is less catalytic reactive than the tunnel structured MnO_2.

Recently, non-radical (e.g., direct electron transfer between PMS-MnO_2 and the substrate) rather than free radical mechanisms were reported in the activation of Oxone by amorphous MnO_2 [26]. To better

understand the mechanisms of the activation of Oxone by MnO_2, ESR experiments with DMPO and TMP as the spin trapping agents were conducted to observe the formation of radicals. DMPO is a spin trapping agent for $SO_4^{·-}$ and $·OH$. No signal was observed in the systems without either PMS or MnO_2 (Figs. 4 and S5). When both MnO_2 and PMS were present, a narrow seven-line (1:2:1:2:1:2:1) spectrum was observed, the signal of 5,5-dimethylpyrroline-(2)-oxyl-(1) (DMPOX), which was the oxidation product of DMPO [33–35]. DMPOX can be generated via the excessive oxidation of DMPO by many strong oxidizing substances such as $SO_4^{·-}$ and $·OH$, as reported in the previous studies [33–35]. Note that the formation of DMPOX did not indicate $SO_4^{·-}$ and $·OH$ were absent [36,37], it mainly indicated that the rate of DMPO oxidation was probably much faster than its rate of trapping radicals in our reaction systems [33]. Therefore, similar to previous research [33], the peak intensity of DMPOX was used to indirectly reflect the amount of free radicals.

For the three crystalline MnO_2 (α-, β- and γ-MnO_2), the intensity of the DMPOX signals significantly decreased when EtOH was added, but only slightly decreased when TBA was added (Fig. 4a–c). This suggested that sulfate radicals played a major role in the oxidation of DMPO, while hydroxyl radicals only played a minor role. For δ-MnO_2, the intensity of DMPOX only slightly decreased when either EtOH or TBA was added (Fig. 4d), indicating that only a negligible or small amount of $SO_4^{·-}$ and $·OH$ was generated in the δ-MnO_2 system.

TMP is a spin trapping agent for $^1O_2$. As shown in Fig. 5, the triplet signals (1:1:1) for TMP-$^1O_2$ were observed in all four types of MnO_2, indicating that $^1O_2$ was formed in the mixtures of Oxone with all four types of MnO_2. The DMPOX formed in δ-MnO_2 might be due to the oxidation of DMPO by $^1O_2$ [38]. Compared with $SO_4^{·-}$ and $·OH$, $^1O_2$ is a mild oxidizing species [26], which might at least partly result in the lower catalytic reactivity of the less crystalline δ-MnO_2 compared with
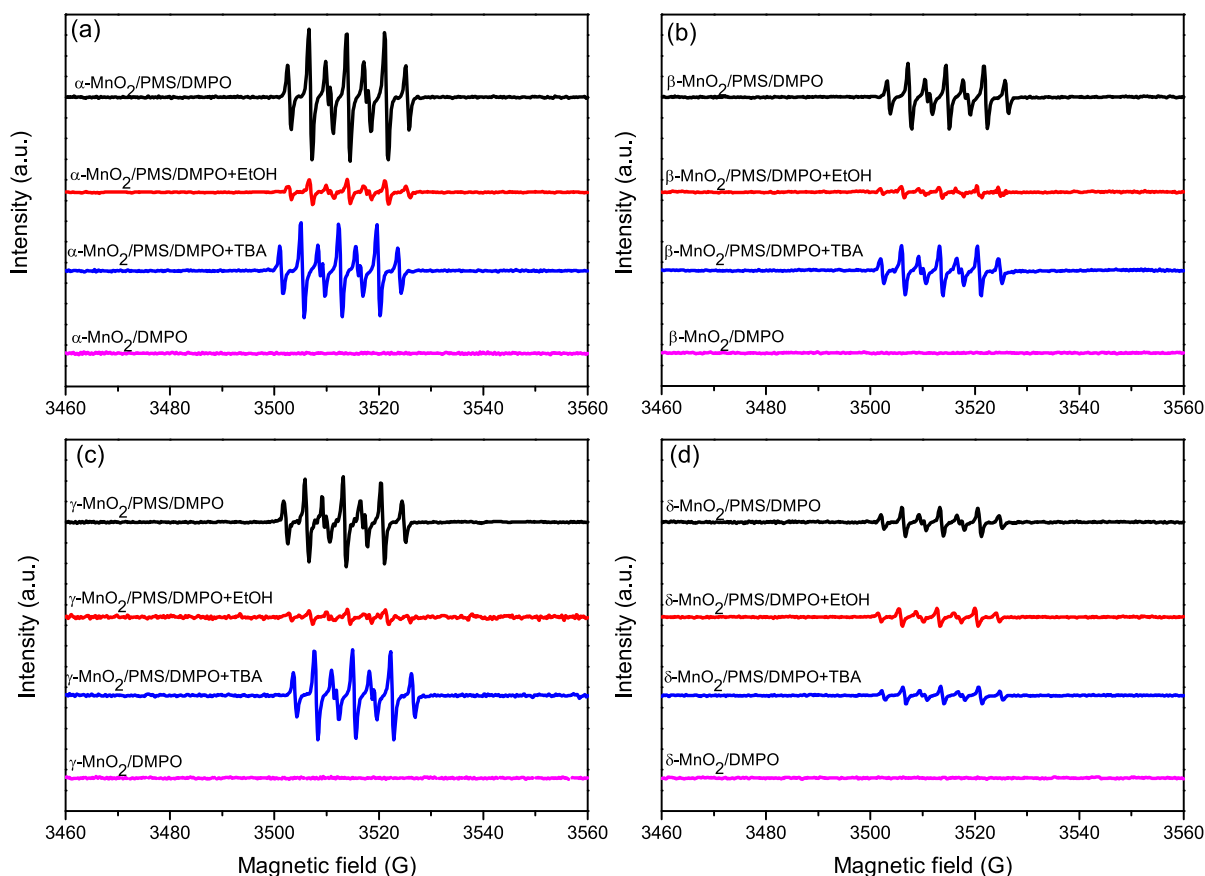

Fig. 4. DMPO spin-trapping ESR spectra of Oxone activated by different MnO_2 with and without the radical quenchers. Conditions: 0.05 g/L catalyst, 1 mM Oxone, 30 mM DMPO, 0.8 M EtOH, and 2 mM TBA.
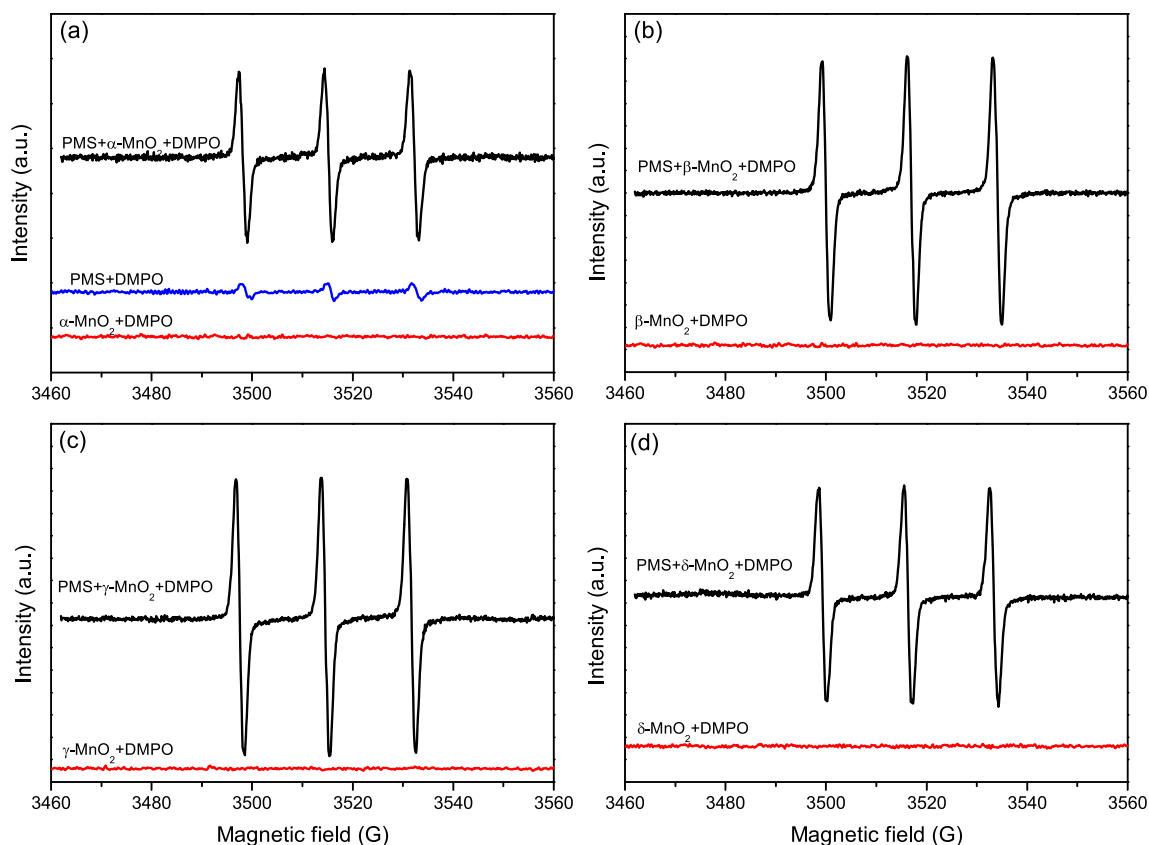
Fig. 5. TMP spin-trapping ESR spectra of Oxone activated by different MnO_2. Conditions: 0.05 g/L catalyst, Oxone 1 mM, TMP 3 mM.

the crystalline MnO_2 (α-, β- and γ-MnO_2). In addition, ESR data did not show the signal for superoxide, indicating that either superoxide was not generated or its concentration was very low [11].

Based on our data and previous research [26], it seems that crystalline MnO_2 can produce more $SO_4^{·-}$ and $·OH$ than less crystalline MnO_2 did, which explained the low catalytic reactivity of δ-MnO_2. In order to better understand what properties affected the efficiency of $SO_4^{·-}$ and $·OH$ generation, many properties were investigated as shown below for crystalline MnO_2, and the properties of the less crystalline MnO_2 (δ-MnO_2) were also examined to see if properties other than crystallinity could affect its catalytic reactivity. Here, in order to better illustrate the relationship between the properties of crystalline MnO_2 and the catalytic reactivity (i.e., k_{tr}-k_{or}), we examined two additional crystalline MnO_2 (α-MnO_2-1 and β-MnO_2-1). The properties of these two MnO_2 were obtained from our previous paper, as shown in Table S2 [22], and their reactivity is shown in Fig. S6.

3.4. Surface physicochemical analysis and the importance of Mn(III) contents

The surface Mn AOS of MnO_2 played an important role in many of its catalytic reactivities [39]. The AOS was obtained by the Mn 3s multiplet splitting spectra method (Fig. 6) based on the following equation: $AOS = 8.95 – 1.13\Delta Es$, where ΔEs is the energy difference between the main peak and its satellite in Mn 3s [40].

Mn surface AOS of α-, β-, γ-, and δ-MnO_2 is 3.63, 3.89, 3.77, and 3.61, respectively (Table 1). The AOS of the four synthesized MnO_2 samples are in the range of 3.6–3.9., which match well with previous reports [16,40]. A chemical titration method was also used to obtain the bulk Mn AOS (Table S1), which is comparable with their respective surface AOS. Except for the layer structured δ-MnO_2 whose reactivity was largely affected by its less crystalline structure as mentioned above, we found that for the crystalline MnO_2, lower surface AOS resulted in

higher reactivity, and a good linear relationship was observed between the catalytic reactivity and the AOS for all five crystalline MnO_2 (Fig. S7a, R2 = 0.97), which is similar to previous studies using MnO_2 as a catalyst in ozone activation and water oxidation [39,41]. This indicates that AOS is important in affecting the activation of Oxone by crystalline MnO_2.

Note that including δ-MnO_2 in the above linear correlation suggested that δ-MnO_2 was an outlier whose poor catalytic reactivity could not be explained by its AOS (data not shown). Similar behaviors were also observed when trying to include δ-MnO_2 in all the other correlation efforts shown below and will not be discussed further.

In addition, Mn(III) has been reported to play an important role in the catalytic reactivity of Mn-based catalysts [16]. For instance, it has
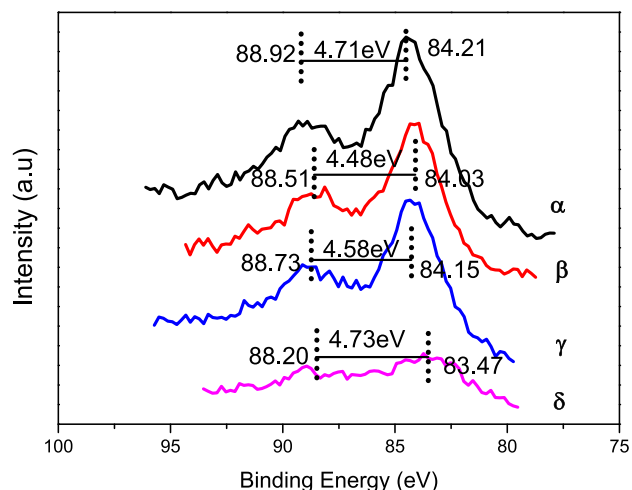

Fig. 6. Mn 3 s XPS spectra of different structured MnO_2.

Table 1
BET surface area, Mn average oxidation state (AOS), and surface Mn and O chemical composition of MnO_2.

MnO_2	Surface area (m^2/g)[a]	AOS[b]	%Mn (III)[c]	%Mn (IV)[c]	%Mn (III)[d]	%Mn (IV)[d]	%O_{sur}[e]	K/Mn[f]
α-MnO_2	175	3.63	25.5	74.5	30.2	69.8	14.7	0.12
β-MnO_2	18	3.89	23.0	77.1	15.3	84.7	20.1	0
γ-MnO_2	73	3.77	24.7	75.3	26.7	73.3	20.1	0
δ-MnO_2	106	3.61	37.9	59.2	40.3	55.1	13.2	0.27

[a] Obtained from Ref. [22].
[b] Obtained from Mn3s multiplet splitting.
[c] Percentage compositions of Mn 3p spectra by fitting Mn(II), Mn(III), and Mn(IV) for the MnO_2 samples before reaction.
[d] Percentage compositions of Mn 3p spectra by fitting Mn(II), Mn(III), and Mn(IV) for the MnO_2 samples after reaction.
[e] Percentage compositions of O 1s spectra by fitting O_{water}, O_{sur}, and O_{latt}.
[f] The ratio of K/Mn was obtained by EDX from Ref. [22].

been shown that Mn(III) has longer (Jahn-Teller distorted) and hence weaker Mn-O bonds than Mn(IV), which results in higher catalytic activity in water oxidation [42,43]. The mechanism of PMS activation by MnO_2 has been proposed in Eqs. (1)–(3). It should be noted that $SO_4^{\cdot -}$ has a higher redox potential than $SO_5^{\cdot -}$ (Eqs. (5) and (6)) [44]. $SO_4^{\cdot -}$ is formed from PMS activation by Mn(III) (Eq. (2)), while $SO_5^{\cdot -}$ forms from PMS activation by Mn(IV) (Eq. (1)) [44], thus higher Mn(III) content in MnO_2 should lead to higher reactivity.

$$SO_5^- + e \rightarrow SO_5^{2-} \quad E^0 = 1.10 \quad (5)$$

$$SO_4^- + e \rightarrow SO_4^{2-} \quad E^0 = 2.60 \quad (6)$$

Based on the obtained Mn 3p spectra (Fig. 7), the Mn(III) content decreased in the order: δ-MnO_2 > α-MnO_2 > γ-MnO_2 > β-MnO_2. When comparing the three crystalline MnO_2, the reactivity decreased in the order α-MnO_2 > γ-MnO_2 > β-MnO_2, which is in the same trend as Mn(III) content. We also observed a reasonable linear relationship

between the catalytic reactivity and the Mn(III) content for the five crystalline MnO_2 (Fig. S7b, $R^2 = 0.61$). Because higher Mn(III) content would lead to lower AOS, it is not surprising that we observed similar linear relationships between the catalytic reactivity and AOS or Mn(III) content. However, the linear relationship between catalytic reactivity and Mn(III) is not as good as that between catalytic reactivity and AOS ($R^2 = 0.97$). It is possible that the mixed Mn valance (III/IV) in MnO_2 is important in its catalytic reactivity [16,45–49]. However, the optimum ratio of Mn(III)/Mn(IV) for the activation of PMS needs further study.

Moreover, oxygen species on MnO_2 surfaces have been reported to affect its catalytic and oxidative reactivity [50,51]. In order to understand how oxygen species affected the activation of PMS, O1s XPS spectra were obtained, which can be deconvoluted into two species based on the peak positions, including lattice oxygen (O_{latt}) between [529.0–529.8 eV] and surface adsorbed oxygen (O_{sur}) between [531.0–532.0 eV] [40,52]. In our synthesized MnO_2, there were two types of oxygen species (Fig. S8). The abundance of lattice oxygen species decreased in the order: δ-MnO_2 > α-MnO_2 > β-MnO_2 ≈ γ-MnO_2 (Table S1), while that of surface adsorbed oxygen species increased in the order: δ-MnO_2 < α-MnO_2 < β-MnO_2 ≈ γ-MnO_2. No linear correlation between the catalytic reactivity and surface adsorbed oxygen species (Fig. S7c, $R^2 = 0.33$) or lattice oxygen species (Fig. S7d, $R^2 = 0.33$) was observed in our experiments, indicating that the oxygen species were not the main factor affecting the activation of PMS.

3.5. Electrochemical impedance spectroscopy (EIS) of MnO_2

Another important factor affecting the catalytic reactivity is the interfacial conductivity of the catalyst. Previous studies have shown that lower charge resistance of MnO_2 would lead to higher oxygen evolution reactivity [16]. The charge transfer resistance of different structured MnO_2 was obtained by an equivalent circuit with $C_2/R_2 + R_1$ (Fig. S9 and Table S3). Based on the EIS spectra (Fig. 8), the conductivity as indicated by the R_2 values decreases in the order: α-MnO_2 > δ-MnO_2 > γ-MnO_2 > β-MnO_2. For the five crystalline MnO_2, we observed a good linear relationship between catalytic
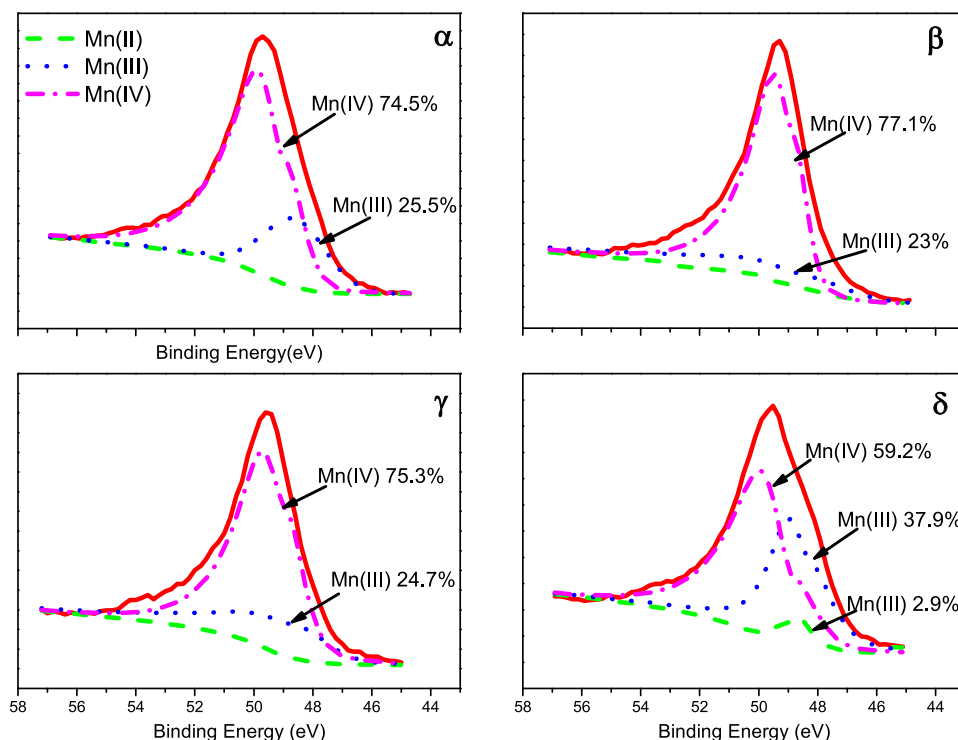

Fig. 7. Mn 3p XPS spectra for different structured MnO_2 by fitting Mn(II), Mn(III), and Mn(IV) reference spectra. Note that the red solid lines stand for the experimentally observed spectra of MnO_2. (For interpretation of the references to colour in this figure legend, the reader is referred to the web version of this article.)
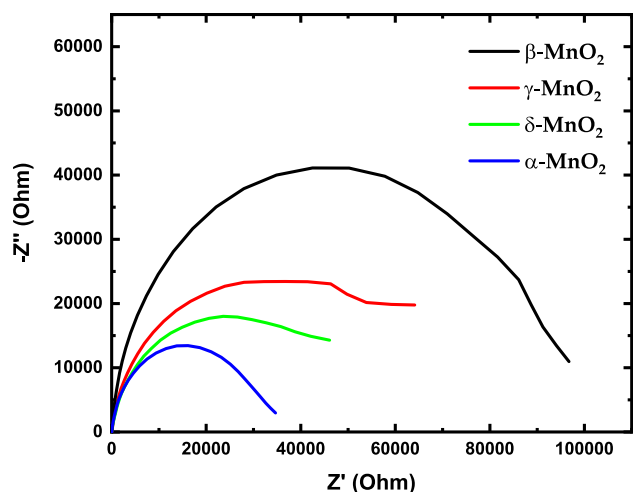
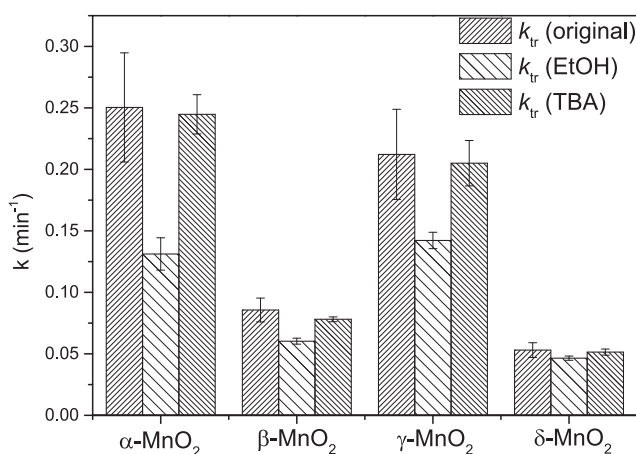**Fig. 8.** Nyquist plots obtained from EIS measurements of the MnO_2.

Fig. 9. Reaction rate constants with and without EtOH (0.8 M) or TBA (2 mM) as the quenching agents. Reaction conditions: [BPA] = 6 μM, MnO_2 = 0.05 g/L, Oxone = 1 mM, and pH = 3.07 ± 0.04.
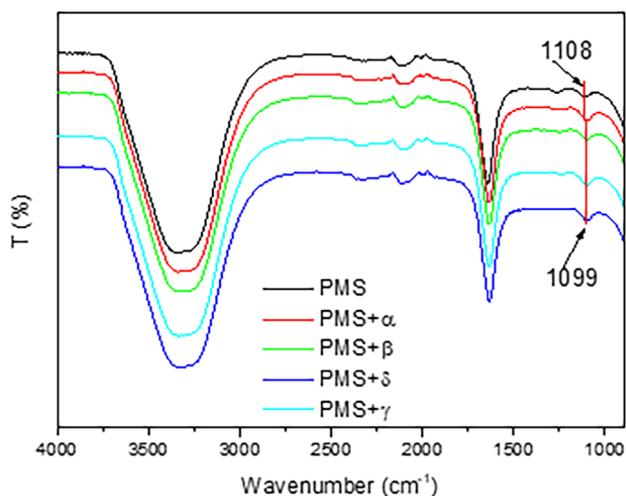

Fig. 10. ATR-FTIR spectra of PMS solution without MnO_2 and different structured MnO_2 in PMS solution.

reactivity and resistance (Fig. S7e, R^2 = 0.91), indicating the conductivity of MnO_2 was important in affecting the activation of PMS. Low charge resistance would favor electron transfer, which increased the reactivity.

3.6. Role of MnO_2 structures

As reported, α-, β-, and γ-MnO_2 contain different types of tunnel structures, which might partially affect their catalytic reactivity. α-MnO_2 has a large (2 × 2) tunnel structure containing both edge-shared and corner-shared MnO_6. γ-MnO_2 has (1 × 1) and (1 × 2) tunnel structures also containing both edge-shared and corner-shared MnO_6. β-MnO_2 only contains small tunnel structures (1 × 1) with corner-shared MnO_6 [53]. Among the tunnel-structured MnO_2, the catalytic reactivity of α- and γ-MnO_2 was much higher than that of the single-tunnel structured β-MnO_2, mostly due to the larger tunnel sizes [15,54]. Although layer structured δ-MnO_2 has more accessible sites, its poor crystallinity resulted in lower catalytic reactivity, as discussed in Section 3.4.

The K^+ content in MnO_2 has been reported to affect the catalytic reactivity [55]. For example, Hou et al. demonstrated that increasing K^+ content in OMS-2 resulted in enhancement in benzene oxidation [55]. As shown in Table 1, the K/Mn ratio of MnO_2 decreased in the order: δ-MnO_2 > α-MnO_2 > γ-MnO_2 = β-MnO_2, indicating that K^+ content was not the main reason that affected the activation of PMS.

MnO_2 with longer Mn-O bonds have lower Mn-O bond strength, which favors its reactivity [22,42]. The average Mn-O distance of α-, β-, γ- and δ-MnO_2 is 1.925, 1.888, 1.91, and 1.936 Å, respectively [42,56]. For the three tunnel structured MnO_2, longer Mn-O bond length agrees well with higher reactivity. Moreover, surface area (SA) has been believed to be an important factor that correlates with MnO_2 reactivity [57]. In our system, the SA decreased in the order: α-MnO_2 > δ-MnO_2 > γ-MnO_2 > β-MnO_2. However, for the five crystalline MnO_2, we did not observe good linear relationship between the catalytic reactivity and SA (Fig. S7f, R^2 = 0.23), indicating that SA only played a minor role in affecting the activation of Oxone.

3.7. Activation mechanisms of Oxone by MnO_2 under acidic conditions

BPA degradation in PMS-MnO_2 can be ascribed to two reactions, as mentioned earlier. First, it can undergo direct oxidation by MnO_2 especially at more acidic pH (Figs. 2b and 3). For the direct oxidation, different factors including Mn(III) content, reduction potential, surface area, and interfacial conductivity would affect the reactivity [22]. The mechanism of BPA direct oxidation by MnO_2 has been well studied in previous papers [58,59] and will not be addressed here. In addition, the direct oxidation by MnO_2 was negligible at pH 5.5 during the experimental periods (5 min, data not shown). Thus, the catalytic reactivity was approximately the same as the total reactivity (k_{tr}) at pH ≥ 5.5 (Fig. S10).

Second, BPA can be catalytically oxidized by PMS-MnO_2. Based on our ESR analysis, δ-MnO_2 mainly catalyzed PMS to form $^1O_2$, with a negligible or very small amount of $SO_4^{\cdot-}$ or $\cdot OH$ formed; while α-, β- and γ-MnO_2 all catalyzed PMS to form $SO_4^{\cdot-}$, $\cdot OH$ and $^1O_2$. Radical quenching tests by two scavengers namely ethanol (EtOH) and TBA were thus conducted to examine the relative importance of the free radicals. EtOH has been employed as a quenching agent for both $SO_4^{\cdot-}$ and $\cdot OH$ because of its high second order reaction rate constant with $SO_4^{\cdot-}$ ($3.5 \times 10^7 M^{-1}s^{-1}$) and $\cdot OH$ ($1.9 \times 10^9 M^{-1}s^{-1}$) [60]. TBA is a good quenching agent for $\cdot OH$ because its reaction rate constant with $\cdot OH$ is about 1000 times higher ($6.0 \times 10^8 M^{-1}s^{-1}$) than that with $SO_4^{\cdot-}$ ($4.0 \times 10^5 M^{-1}s^{-1}$) [60].

As shown in Fig. 9, the reactivity was inhibited by EtOH for α-, β-, and γ-MnO_2, but not much affected for δ-MnO_2 due to a negligible or small amount of $SO_4^{\cdot-}$ and $\cdot OH$ formed. However, TBA only slightly inhibited the reactivity for all MnO_2. These results indicated that $SO_4^{\cdot-}$ was the dominant radical for crystalline MnO_2, whereas $\cdot OH$ played a minor role, which agrees with the ESR data and many previous papers [10,18]. Note that BPA radicals were reported to form in the direct oxidation of BPA by MnO_2 [58,59]. However, the control experiments showed that these radicals did not appear to be affected by

the addition of either EtOH or TBA (Fig. S11).

The relative contributions of $SO_4^{\cdot-}$ and $^{\cdot}OH$ to the overall free radical-based oxidation at different reaction times were then calculated based on the amounts of BPA degraded at different times (Fig. 2a) [61]. The detailed explanation of how the contributions were calculated is included in Text S3. As shown in Text S3, the contribution of $SO_4^{\cdot-}$ was 90.1–97.0%, 69.2–91.8%, and 76.1–90.1% for α-, β-, and γ-MnO$_2$, respectively. Previous studies have shown that compared with $^{\cdot}OH$, $SO_4^{\cdot-}$ is a more efficient and selective oxidant for organic compounds containing unsaturated bonds and aromatic constituents [3]. Therefore, the largest contribution of $SO_4^{\cdot-}$ for α-MnO$_2$ can at least partially explain its highest catalytic reactivity.

After subtracting BPA degradation by both radicals ($SO_4^{\cdot-}$ and $^{\cdot}OH$) and by direct oxidation by MnO$_2$, there is still significant BPA degradation (Figs. 2b and 9). This suggests that there are other reaction mechanisms in the system. ESR analysis also showed that $^1O_2$ formed in PMS-MnO$_2$. $^1O_2$ is a mild oxidant and is resistant to saturated alcohols (e.g., methanol and TBA) [62]. Singlet oxygen was reported to form through the following mechanism [63,64].

$$2HO^{\cdot} \rightarrow \frac{1}{2}{}^1O_2 + H_2O \tag{7}$$

In addition, ATR-FTIR was employed to demonstrate possible complexes formed on the surface of MnO$_2$ (Fig. 10). For PMS alone, the peaks in the range of 900–1340 cm^{-1} are generally assigned to the symmetric and asymmetric stretching of the S–O bond in either HSO_5^- or SO_4^{2-} [11,65]. There was a blue shift of about 9 cm^{-1} to the position of 1099 cm^{-1} when MnO$_2$ was added into the PMS solution. Previous studies assigned the shift to the formation of complexes such as $[MnO-(HO)OSO_3^-]$ on the MnO$_2$ surface [65]. However, we also observed a similar shift for δ-MnO$_2$. Considering the poor catalytic activity of δ-MnO$_2$ in activating PMS, the formation of surface complexes itself does not seem to support efficient catalytic reactivity.

Moreover, the XPS spectra of different Mn-based catalysts after reaction under acidic conditions were obtained (Table 1 and Table S1 and Fig. S12). As demonstrated in previous studies [34], the abundance of Mn(IV) on Mn-based catalysts increased whereas that of Mn(III) decreased after the catalytic activation of Oxone at pH 7. However, we observed different results. For α-, γ- and δ-MnO$_2$, the abundance of Mn(III) increased and that of Mn(IV) decreased. Whereas for β-MnO$_2$, the abundance of Mn(III) slightly decreased and that of Mn(IV) increased. We believed that this is because both direct oxidation and catalytic oxidation were involved in the reactions. For catalytic reaction, it has been shown that the abundance of Mn(III) decreased whereas that of Mn(IV) increased [34,66]. For direct oxidation, it has been shown that the abundance of Mn(III) increased while that of Mn(IV) decreased [67]. Therefore, the Mn(III) content of β-MnO$_2$ decreased due to the small contribution of direct oxidation. For δ-MnO$_2$, direct oxidation played a dominant role, which decreased the abundance of Mn(IV) [67]. Whereas for α- and γ-MnO$_2$, both mechanisms played an important role in the total reactivity, resulting in the above phenomenon. Therefore, the results obtained from a previous study [11] using XPS to analyze the change in the Mn valence after reaction under acidic conditions should be carefully re-interpreted because direct oxidation was not considered.

4. Conclusions

In this study, four MnO$_2$ with different structures were synthesized and tested in the activation of PMS for the degradation of BPA as a representative contaminant. The catalytic performance decreased in the order: α-MnO$_2$ > γ-MnO$_2$ > β-MnO$_2$ > δ-MnO$_2$. The lowest catalytic reactivity of δ-MnO$_2$ was mainly due to its low extent of crystallinity. For the crystalline structured MnO$_2$, lower Mn AOS, higher Mn(III) content, and higher conductivity all correlated well with higher reactivity. Under acidic pH, BPA degradation underwent three

mechanisms: (1) catalytic oxidation by radicals ($SO_4^{\cdot-}$ and $^{\cdot}OH$); (2) direct oxidation by MnO2; and (3) catalytic reaction by nonradical mechanisms, such as $^1O_2$. For the crystalline structured MnO$_2$ (α-, β-, and γ-MnO$_2$), BPA degradation was dominated by the radical mechanism, while for the less crystalline δ-MnO$_2$, direct oxidation played an important role. In addition, sulfate radical is more important than hydroxyl radical in the radical mechanism. Finally, the observed reactivity in contaminant degradation under acidic conditions is a combination of catalytic and direct oxidation. When interpreting the reported reactivity data, care should be taken when the solution pH of the Mn oxide controls were not properly adjusted.

Appendix A. Supplementary data

Supplementary data to this article can be found online at https://doi.org/10.1016/j.cej.2019.03.238.

References

[1] F. Ghanbari, M. Moradi, Application of peroxymonosulfate and its activation methods for degradation of environmental organic pollutants: Review, Chem. Eng. J. 310 (Part 1) (2017) 41–62.

[2] G.P. Anipsitakis, D.D. Dionysiou, Radical generation by the interaction of transition metals with common oxidants, Environ. Sci. Technol. 38 (2004) 3705–3712.

[3] P. Hu, M. Long, Cobalt-catalyzed sulfate radical-based advanced oxidation: a review on heterogeneous catalysts and applications, Appl. Catal. B 181 (2016) 103–117.

[4] J. Wang, S. Wang, Activation of persulfate (PS) and peroxymonosulfate (PMS) and application for the degradation of emerging contaminants, Chem. Eng. J. 334 (2018) 1502–1517.

[5] X. Lu, T. Zhai, X. Zhang, Y. Shen, L. Yuan, B. Hu, L. Gong, J. Chen, Y. Gao, J. Zhou, WO$_{3-x}$@Au@ MnO$_2$ core-shell nanowires on carbon fabric for high-performance flexible supercapacitors, Adv. Mater. 24 (2012) 938–944.

[6] S. Taujale, L.R. Baratta, J. Huang, H. Zhang, Interactions in ternary mixtures of MnO$_2$, Al$_2$O$_3$, and natural organic matter (NOM) and the impact on MnO$_2$ oxidative reactivity, Environ. Sci. Technol. 50 (2016) 2345–2353.

[7] R. Radhakrishnan, S.T. Oyama, Ozone decomposition over manganese oxide supported on ZrO$_2$ and TiO$_2$: a kinetic study using in situ laser Raman spectroscopy, J. Catal. 199 (2001) 282–290.

[8] J. Chen, J.C. Lin, V. Purohit, M.B. Cutlip, S.L. Suib, Photoassisted catalytic oxidation of alcohols and halogenated hydrocarbons with amorphous manganese oxides, Catal. Today 33 (1997) 205–214.

[9] H. Zhou, Y. Shen, J. Wang, X. Chen, C.-L. O'Young, S.L. Suib, Studies of decomposition of H$_2$O$_2$ over manganese oxide octahedral molecular sieve materials, J. Catal. 176 (1998) 321–328.

[10] S. Luo, L. Duan, B. Sun, M. Wei, X. Li, A. Xu, Manganese oxide octahedral molecular sieve (OMS-2) as an effective catalyst for degradation of organic dyes in aqueous solutions in the presence of peroxymonosulfate, Appl. Catal. B 164 (2015) 92–99.

[11] A. Khan, H. Wang, Y. Liu, A. Jawad, J. Ifthikar, Z. Liao, T. Wang, Z. Chen, Highly efficient α-Mn$_2$O$_3$@α-MnO$_2$-500 nanocomposite for peroxymonosulfate activation: comprehensive investigation of manganese oxides, J. Mater. Chem. A 6 (2018) 1590–1600.

[12] E. Saputra, S. Muhammad, H. Sun, H.M. Ang, M. Tade, S. Wang, Different crystallographic one-dimensional MnO$_2$ nanomaterials and their superior performance in catalytic phenol degradation, Environ. Sci. Technol. 47 (2013) 5882–5887.

[13] E. Saputra, S. Muhammad, H. Sun, H.-M. Ang, M.O. Tadé, S. Wang, Manganese oxides at different oxidation states for heterogeneous activation of peroxymonosulfate for phenol degradation in aqueous solutions, Appl. Catal. B 142 (2013) 729–735.

[14] E. Saputra, S. Muhammad, H. Sun, H.-M. Ang, M.O. Tadé, S. Wang, Shape-controlled activation of peroxymonosulfate by single crystal α-Mn$_2$O$_3$ for catalytic phenol degradation in aqueous solution, Appl. Catal. B 154 (2014) 246–251.

[15] J. Zhang, Y. Li, L. Wang, C. Zhang, H. He, Catalytic oxidation of formaldehyde over manganese oxides with different crystal structures, Catal. Sci. Technol. 5 (2015) 2305–2313.

[16] Y. Meng, W. Song, H. Huang, Z. Ren, S.-Y. Chen, S.L. Suib, Structure–property relationship of bifunctional MnO₂ nanostructures: highly efficient, ultra-stable electrochemical water oxidation and oxygen reduction reaction catalysts identified in alkaline media, JACS 136 (2014) 11452–11464.

[17] H. Zhang, C.-H. Huang, Oxidative transformation of triclosan and chlorophene by manganese oxides, Environ. Sci. Technol. 37 (2003) 2421–2430.

[18] Y. Wang, H. Sun, H.M. Ang, M.O. Tadé, S. Wang, 3D-hierarchically structured MnO₂ for catalytic oxidation of phenol solutions by activation of peroxymonosulfate: structure dependence and mechanism, Appl. Catal. B 164 (2015) 159–167.

[19] D. Tang, G. Zhang, S. Guo, Efficient activation of peroxymonosulfate by manganese oxide for the degradation of azo dye at ambient condition, J. Colloid Interface Sci. 454 (2015) 44–51.

[20] W.-C. Peng, S.-B. Wang, X.-Y. Li, Shape-controlled synthesis of one-dimensional α-MnO₂ nanocrystals for organic detection and pollutant degradation, Sep. Purif. Technol. 163 (2016) 15–22.

[21] J. Deng, S. Feng, X. Ma, C. Tan, H. Wang, S. Zhou, T. Zhang, J. Li, Heterogeneous degradation of Orange II with peroxymonosulfate activated by ordered mesoporous MnFe₂O₄, Sep. Purif. Technol. 167 (2016) 181–189.

[22] J. Huang, S. Zhong, Y. Dai, C.-C. Liu, H. Zhang, Effect of MnO₂ phase structure on the oxidative reactivity toward bisphenol A degradation, Environ. Sci. Technol. 52 (2018) 11309–11318.

[23] A. Belfroid, M. van Velzen, B. van der Horst, D. Vethaak, Occurrence of bisphenol A in surface water and uptake in fish: evaluation of field measurements, Chemosphere 49 (2002) 97–103.

[24] J.M. Cerrato, M.F. Hochella Jr, W.R. Knocke, A.M. Dietrich, T.F. Cromer, Use of XPS to identify the oxidation state of Mn in solid surfaces of filtration media oxide samples from drinking water treatment plants, Environ. Sci. Technol. 44 (2010) 5881–5886.

[25] S. Lan, X. Wang, Q. Xiang, H. Yin, W. Tan, G. Qiu, F. Liu, J. Zhang, X. Feng, Mechanisms of Mn(II) catalytic oxidation on ferrihydrite surfaces and the formation of manganese (oxyhydr)oxides, Geochim. Cosmochim. Acta 211 (2017) 79–96.

[26] L. Wang, J. Jiang, S.-Y. Pang, J. Zhou, J. Li, S. Sun, Y. Gao, C. Jiang, Oxidation of bisphenol A by nonradical activation of peroxymonosulfate in the presence of amorphous manganese dioxide, Chem. Eng. J. 352 (2018) 1004–1013.

[27] E.-J. Kim, D. Oh, C.-S. Lee, J. Gong, J. Kim, Y.-S. Chang, Manganese oxide nanorods as a robust Fenton-like catalyst at neutral pH: crystal phase-dependent behavior, Catal Today (2016).

[28] T.T. Truong, Y. Liu, Y. Ren, L. Trahey, Y. Sun, Morphological and crystalline evolution of nanostructured MnO2 and its application in lithium-air batteries, ACS Nano 6 (2012) 8067–8077.

[29] E. Saputra, S. Muhammad, H. Sun, A. Patel, P. Shukla, Z. Zhu, S. Wang, α-MnO₂ activation of peroxymonosulfate for catalytic phenol degradation in aqueous solutions, Catal. Commun. 26 (2012) 144–148.

[30] Y. Dai, J.-H. LI, Y. Peng, X.-F. Tang, Effects of MnO₂ crystal structure and surface property on the NH₃-SCR reaction at low temperature, Acta Physico-Chim. Sin. 28 (2012) 1771–1776.

[31] S. Rong, P. Zhang, F. Liu, Y. Yang, Engineering crystal facet of α-MnO₂ nanowire for highly efficient catalytic oxidation of carcinogenic airborne formaldehyde, ACS Catal. 8 (2018) 3435–3446.

[32] L. Yu, G. Zhang, C. Liu, H. Lan, H. Liu, J. Qu, Interface stabilization of undercoordinated iron centers on manganese oxides for nature-inspired peroxide activation, ACS Catal. 8 (2018) 1090–1096.

[33] M. Xie, J. Tang, L. Kong, W. Lu, V. Natarajan, F. Zhu, J. Zhan, Cobalt doped g-C₃N₄ activation of peroxymonosulfate for monochlorophenols degradation, Chem. Eng. J. 360 (2018) 1213–1222.

[34] J. Du, J. Bao, Y. Liu, S.H. Kim, D.D. Dionysiou, Facile preparation of porous Mn/Fe₃O₄ cubes as peroxymonosulfate activating catalyst for effective bisphenol A degradation, Chem. Eng. J. (2018), https://doi.org/10.1016/j.cej.2018.1005.1177.

[35] G.M. Rosen, E.J. Rauckman, Spin trapping of the primary radical involved in the activation of the carcinogen N-hydroxy-2-acetylaminofluorene by cumene hydroperoxide-hematin, Mol. Pharmacol. 17 (1980) 233–238.

[36] S. Maeno, Q. Zhu, M. Sasaki, T. Miyamoto, M. Fukushima, Monopersulfate oxidation of tetrabromobisphenol A by an iron (III)-phthalocyaninetetrasulfate catalyst coordinated to imidazole functionalized silica particles, J. Mol. Catal. A Chem. 400 (2015) 56–63.

[37] J. Fontmorin, R.B. Castillo, W. Tang, M. Sillanpää, Stability of 5, 5-dimethyl-1-pyrroline-N-oxide as a spin-trap for quantification of hydroxyl radicals in processes based on Fenton reaction, Water Res. 99 (2016) 24–32.

[38] S. Zhu, X. Li, J. Kang, X. Duan, S. Wang, Persulfate activation on crystallographic manganese oxides: mechanism of singlet oxygen evolution for nonradical selective degradation of aqueous contaminants, Environ. Sci. Technol. 53 (2019) 307–315.

[39] I.G. McKendry, S.K. Kondaveeti, S.L. Shumlas, D.R. Strongin, M.J. Zdilla, Decoration of the layered manganese oxide birnessite with Mn (II/III) gives a new water oxidation catalyst with fifty-fold turnover number enhancement, Dalton Trans. 44 (2015) 12981–12984.

[40] J. Wan, L. Zhou, H. Deng, F. Zhan, R. Zhang, Oxidative degradation of sulfamethoxazole by different MnO₂ nanocrystals in aqueous solution, J. Mol. Catal. A Chem. 407 (2015) 67–74.

[41] F. Nawaz, H. Cao, Y. Xie, J. Xiao, Y. Chen, Z.A. Ghazi, Selection of active phase of MnO₂ for catalytic ozonation of 4-nitrophenol, Chemosphere 168 (2017) 1457–1466.

[42] D.M. Robinson, Y.B. Go, M. Mui, G. Gardner, Z. Zhang, D. Mastrogiovanni, E. Garfunkel, J. Li, M. Greenblatt, G.C. Dismukes, Photochemical water oxidation by crystalline polymorphs of manganese oxides: structural requirements for catalysis, JACS 135 (2013) 3494–3501.

[43] U. Maitra, B. Naidu, A. Govindaraj, C. Rao, Importance of trivalency and the eg1 configuration in the photocatalytic oxidation of water by Mn and Co oxides, Proc. Natl. Acad. Sci. U.S.A. 110 (2013) 11704–11707.

[44] W.-D. Oh, Z. Dong, T.-T. Lim, Generation of sulfate radical through heterogeneous catalysis for organic contaminants removal: current development, challenges and prospects, Appl. Catal. B 194 (2016) 169–201.

[45] A. Indra, P.W. Menezes, I. Zaharieva, E. Baktash, J. Pfrommer, M. Schwarze, H. Dau, M. Driess, Active mixed-valent mnox water oxidation catalysts through partial oxidation (corrosion) of nanostructured MnO particles, Angew. Chem. Int. Edition 52 (2013) 13206–13210.

[46] I. Zaharieva, P. Chernev, M. Risch, K. Klingan, M. Kohlhoff, A. Fischer, H. Dau, Electrosynthesis, functional, and structural characterization of a water-oxidizing manganese oxide, Energy Environ. Sci. 5 (2012) 7081–7089.

[47] H. Peng, I.G. McKendry, R. Ding, A.C. Thenuwara, Q. Kang, S.L. Shumlas, D.R. Strongin, M.J. Zdilla, J.P. Perdew, Redox properties of birnessite from a defect perspective, Proc. Natl. Acad. Sci. U.S.A. 114 (2017) 9523–9528.

[48] N. Birkner, S. Nayeri, B. Pashaei, M.M. Najafpour, W.H. Casey, A. Navrotsky, Energetic basis of catalytic activity of layered nanophase calcium manganese oxides for water oxidation, Proc. Natl. Acad. Sci. U.S.A. 110 (2013) 8801–8806.

[49] D.R. Kolling, N. Cox, G.M. Ananyev, R.J. Pace, G.C. Dismukes, What are the oxidation states of manganese required to catalyze photosynthetic water oxidation? Biophys. J. 103 (2012) 313–322.

[50] B. Zhao, R. Ran, X. Wu, D. Weng, Phase structures, morphologies, and NO catalytic oxidation activities of single-phase MnO₂ catalysts, Appl. Catal. A 514 (2016) 24–34.

[51] J. Li, R. Wang, J. Hao, Role of lattice oxygen and lewis acid on ethanol oxidation over OMS-2 catalyst, J. Phys. Chem. C 114 (2010) 10544–10550.

[52] F. Wang, H. Dai, J. Deng, G. Bai, K. Ji, Y. Liu, Manganese oxides with rod-, wire-, tube-, and flower-like morphologies: highly effective catalysts for the removal of toluene, Environ. Sci. Technol. 46 (2012) 4034–4041.

[53] V.B.R. Boppana, S. Yusuf, G.S. Hutchings, F. Jiao, Nanostructured alkaline-cation-containing δ-MnO₂ for photocatalytic water oxidation, Adv. Funct. Mater. 23 (2013) 878–884.

[54] T. Chen, H. Dou, X. Li, X. Tang, J. Li, J. Hao, Tunnel structure effect of manganese oxides in complete oxidation of formaldehyde, Microporous Mesoporous Mater. 122 (2009) 270–274.

[55] J. Hou, L. Liu, Y. Li, M. Mao, H. Lv, X. Zhao, Tuning the K⁺ concentration in the tunnel of OMS-2 nanorods leads to a significant enhancement of the catalytic activity for benzene oxidation, Environ. Sci. Technol. 47 (2013) 13730–13736.

[56] S. Liang, F. Teng, G. Bulgan, R. Zong, Y. Zhu, Effect of phase structure of MnO₂ nanorod catalyst on the activity for CO oxidation, J. Phys. Chem. C 112 (2008) 5307–5315.

[57] J.Y. Shin, M.A. Cheney, Abiotic transformation of atrazine in aqueous suspension of four synthetic manganese oxides, Colloids Surf. A Physicochem. Eng. Asp. 242 (2004) 85–92.

[58] K. Lin, W. Liu, J. Gan, Oxidative removal of bisphenol A by manganese dioxide: efficacy, products, and pathways, Environ. Sci. Technol. 43 (2009) 3860–3864.

[59] J. Im, C.W. Prevatte, S.R. Campagna, F.E. Löffler, Identification of 4-hydroxycumyl alcohol as the major MnO₂-mediated bisphenol A transformation product and evaluation of its environmental fate, Environ. Sci. Technol. 49 (2015) 6214–6221.

[60] G.-X. Huang, C.-Y. Wang, C.-W. Yang, P.-C. Guo, H.-Q. Yu, Degradation of Bisphenol A by peroxymonosulfate catalytically activated with Mn₁.₈Fe₁.₂O₄ nanospheres: synergism between Mn and Fe, Environ. Sci. Technol. 51 (2017) 12611–12618.

[61] B. Jiang, Y. Liu, J. Zheng, M. Tan, Z. Wang, M. Wu, Synergetic transformations of multiple pollutants driven by Cr(VI)–sulfite reactions, Environ. Sci. Technol. 49 (2015) 12363–12371.

[62] X. Duan, H. Sun, Z. Shao, S. Wang, Nonradical reactions in environmental remediation processes: uncertainty and challenges, Appl. Catal. B 224 (2018) 973–982.

[63] C. Li, J. Wu, W. Peng, Z. Fang, J. Liu, Peroxymonosulfate activation for efficient sulfamethoxazole degradation by Fe₃O₄/β-FeOOH nanocomposites: coexistence of radical and non-radical reactions, Chem. Eng. J. 356 (2019) 904–914.

[64] H. Lin, S. Li, B. Deng, W. Tan, R. Li, Y. Xu, H. Zhang, Degradation of bisphenol A by activating peroxymonosulfate with Mn₀.₆Zn₀.₄Fe₂O₄ fabricated from spent Zn-Mn alkaline batteries, Chem. Eng. J. 364 (2019) 541–551.

[65] Y. Ren, L. Lin, J. Ma, J. Yang, J. Feng, Z. Fan, Sulfate radicals induced from peroxymonosulfate by magnetic ferrospinel MFe₂O₄ (M=Co, Cu, Mn, and Zn) as heterogeneous catalysts in the water, Appl. Catal. B 165 (2015) 572–578.

[66] J. Xie, Y. Wei, X. Song, Y. Chen, Q. Zou, M. Wang, A. Xu, X. Li, Controlled growth of γ-MnO₂ nanoflakes on OMS-2 for efficient decomposition of organic dyes in aqueous solution via peroxymonosulfate activation, J. Colloid Interface Sci. 529 (2018) 476–482.

[67] N. Shaikh, Saru Taujale, H. Zhang, K. Artyushkova, A.S. Ali, J.M. Cerrato, Spectroscopic investigation of interfacial interaction of manganese oxide with triclosan, aniline, and phenol, Environ. Sci. Technol. 50 (2016) 10978–10987.